FIGURES

in

Statistics of Medical Imaging

by

Tianhu Lei

1

Introduction

2

There are no figures in this chapter.

2

x-ray CT Physics and Mathematics

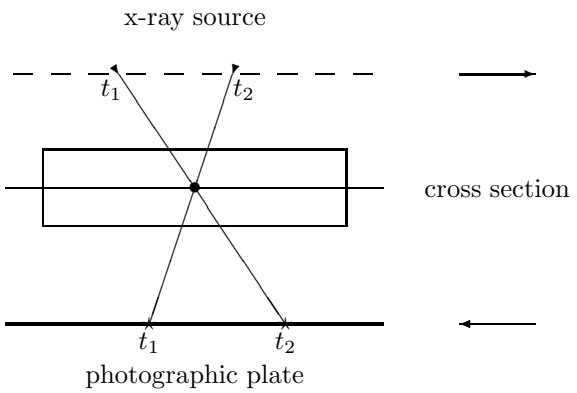

FIGURE 2.1
Linear tomography. t_1 and t_2 denote the time instants. $\longrightarrow$ represents the moving direction.

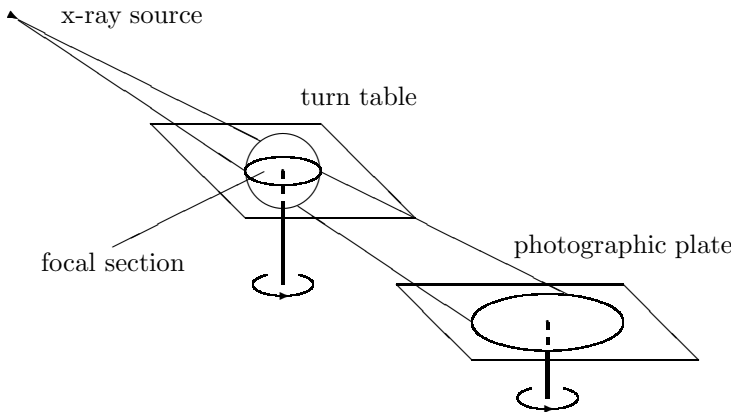

FIGURE 2.2
Transaxial tomography. $\rightarrow$ represents the rotating direction.

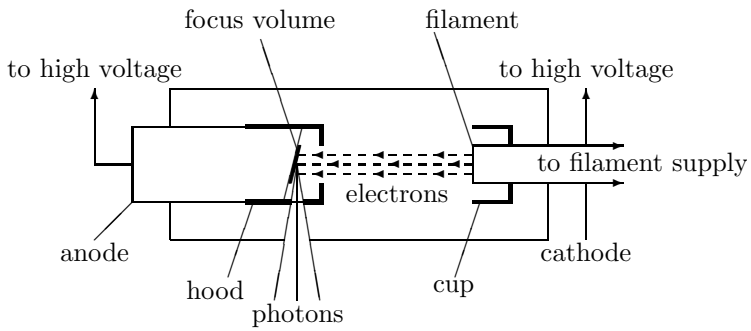

FIGURE 2.3
An illustration of x-ray tube and photon emission.

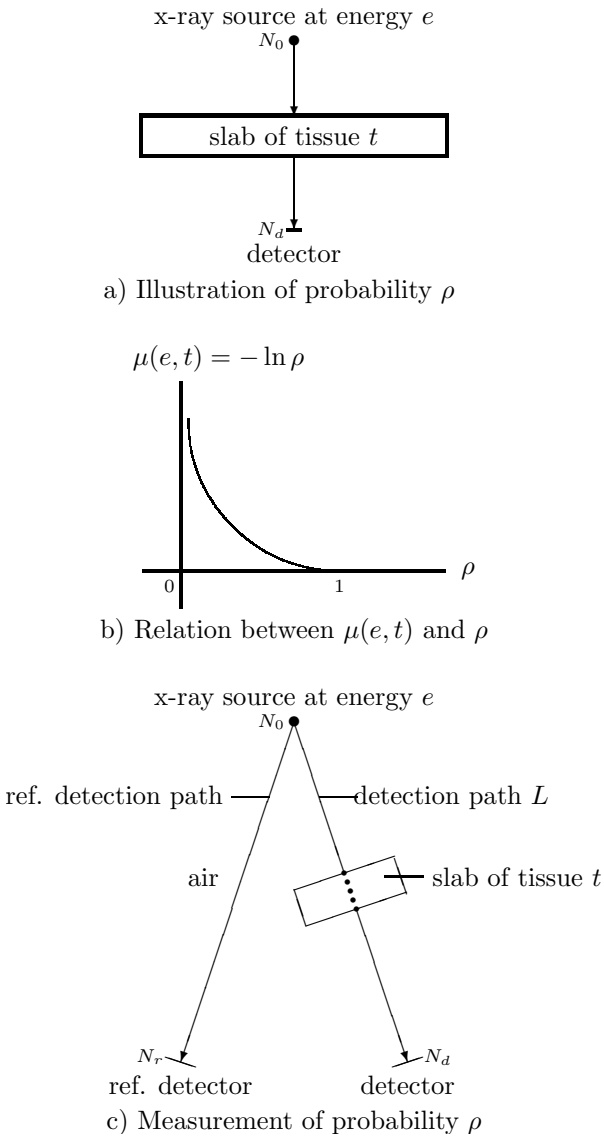

FIGURE 2.4
An illustration for the linear attenuation coefficient of x-ray.

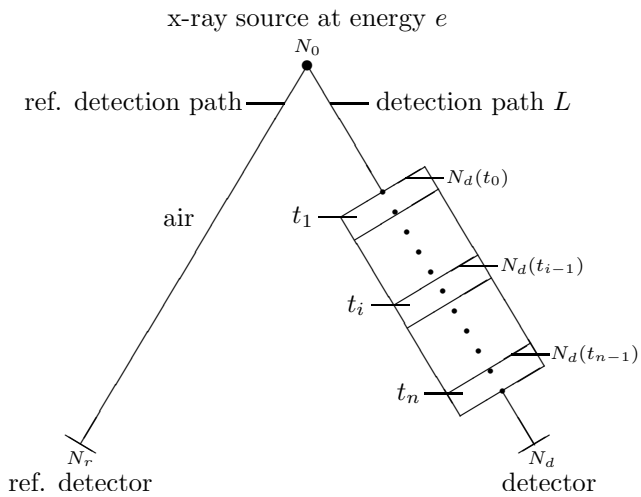

FIGURE 2.5
An illustration of the relative linear attenuation coefficient of x-ray.

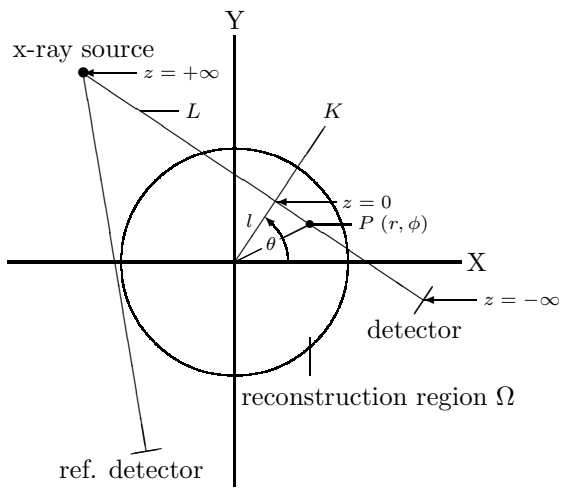

FIGURE 2.6
An illustration of the projection.

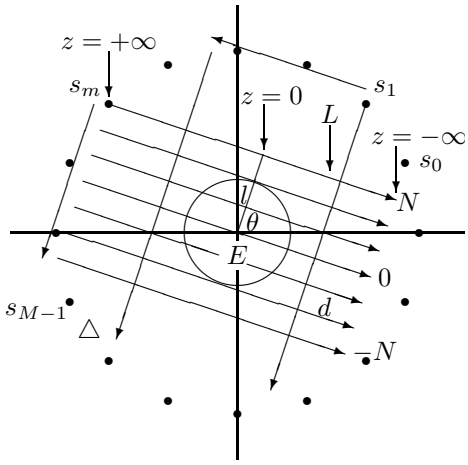

FIGURE 2.7
Parallel projections of the data collection in x-ray CT.

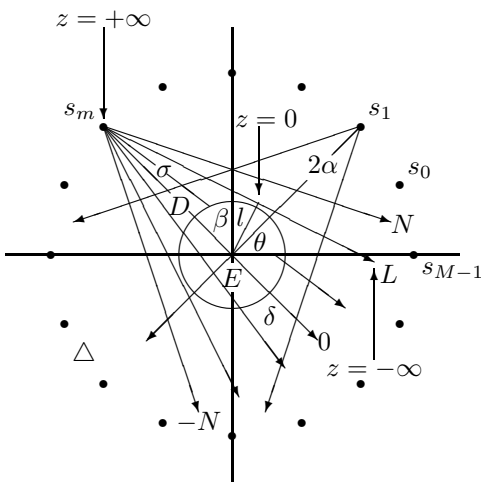

FIGURE 2.8
Divergent projections of the data collection in x-ray CT.

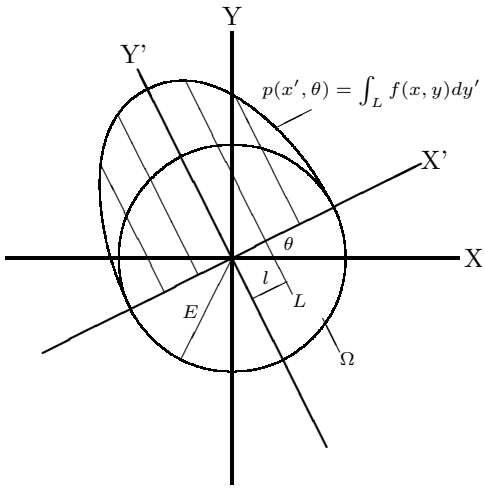

FIGURE 2.9
An illustration for Fourier slice theorem.

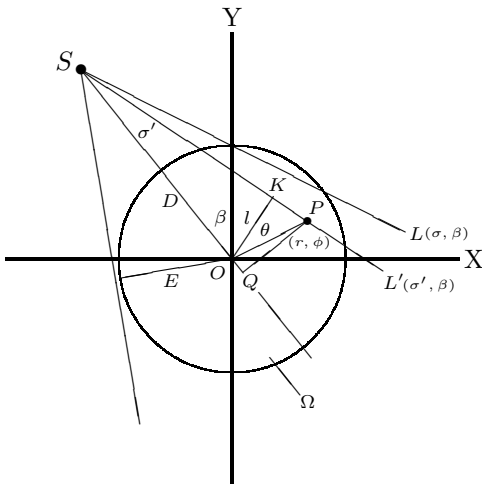

FIGURE 2.10
An illustration of the geometry for the convolution of divergent projections.

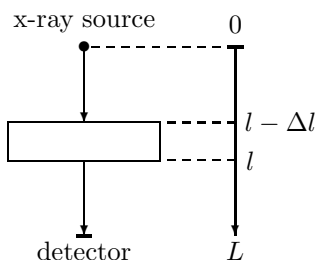

FIGURE 2.11
Physical mechanisms for illustrating the attenuation coefficient.

3

MRI Physics and Mathematics

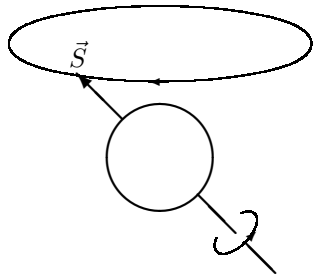

FIGURE 3.1
A spin and the spin angular momentum $\vec{S}$.

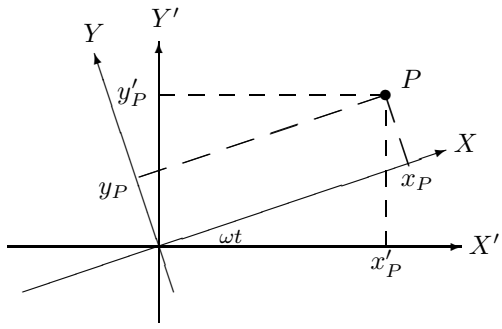

FIGURE 3.2
The fixed reference frame {X,Y,Z} and the rotating reference frame $\{\mathrm{X}', \mathrm{Y}', \mathrm{Z}'\}$ have the same vertical axis. The horizontal plane $\{\mathrm{X}', \mathrm{Y}'\}$ is rotating about the vertical axis in the clockwise direction.

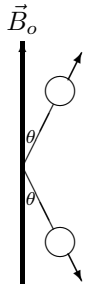

FIGURE 3.3
The alignment of nuclear spins in a static, external magnetic field.

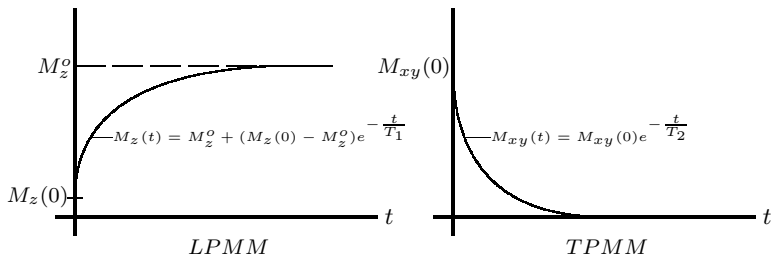

FIGURE 3.4
The dynamic behavior of the longitudinal and the transverse macroscopic magnetization.

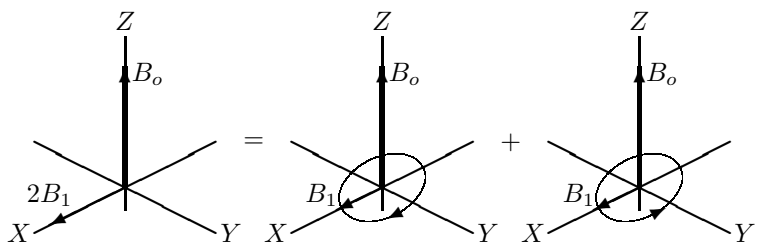

FIGURE 3.5
A linear polarized field is decomposed into two counter-rotating circularly polarized fields.

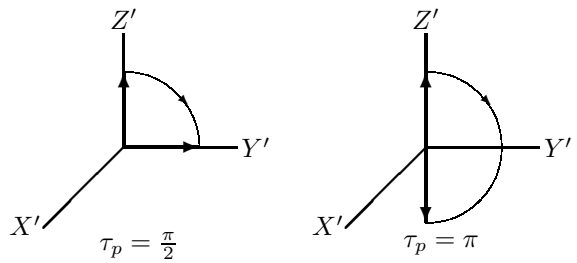

FIGURE 3.6
$(\frac{\pi}{2})_{x'}$ and $(\pi)_{x'}$ excitation pulses flip TEMM.

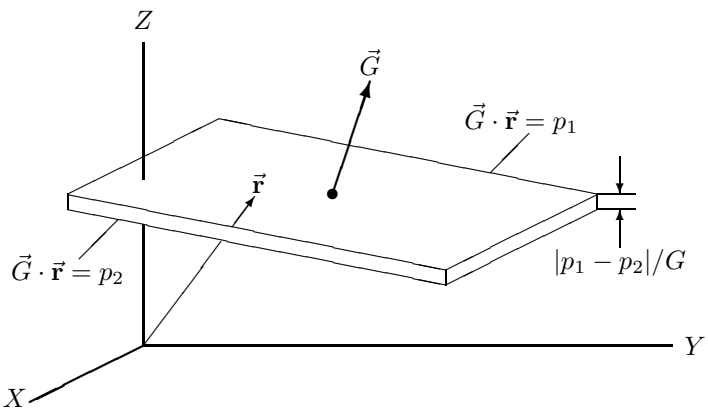

FIGURE 3.7
Mathematical expressions of the plane and the slice.

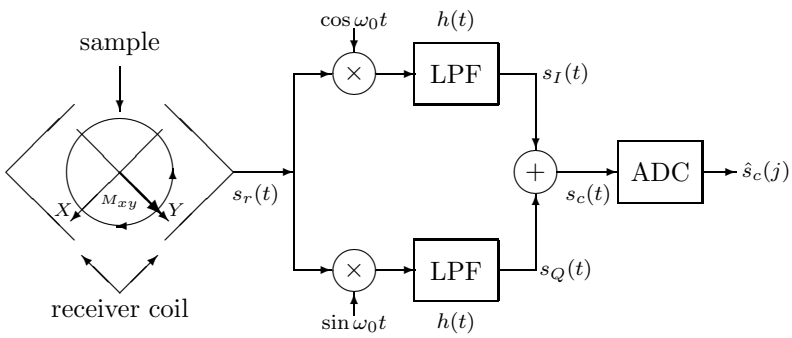

FIGURE 3.8
MR signal detection and demodulation. In this simplified signal flow diagram, $s_r(t)$, $s_c(t)$, and $\hat{s}_c(j)$ represent the pure signal components, the corresponding noise components are not included.

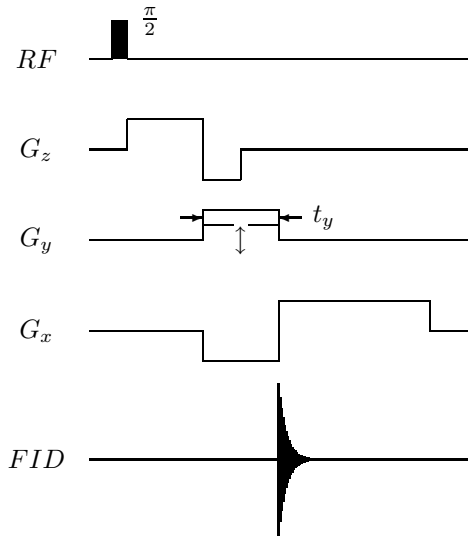

FIGURE 3.9
A timing diagram in the rectilinear k-space sampling.

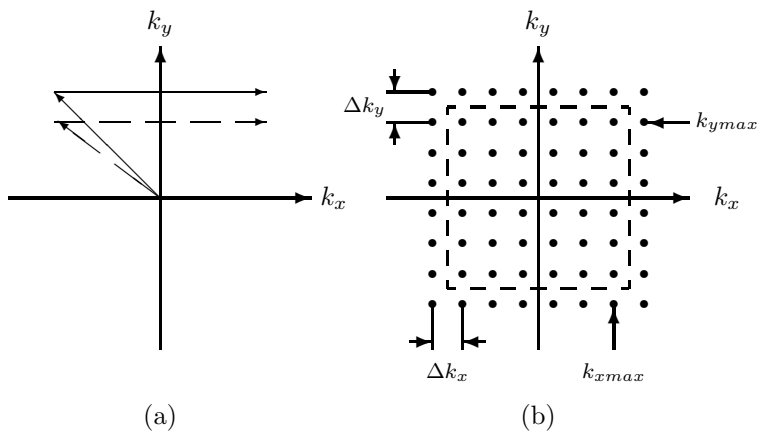

FIGURE 3.10
The trajectory (a) and the sampling (b) in the rectilinear k-space sampling.

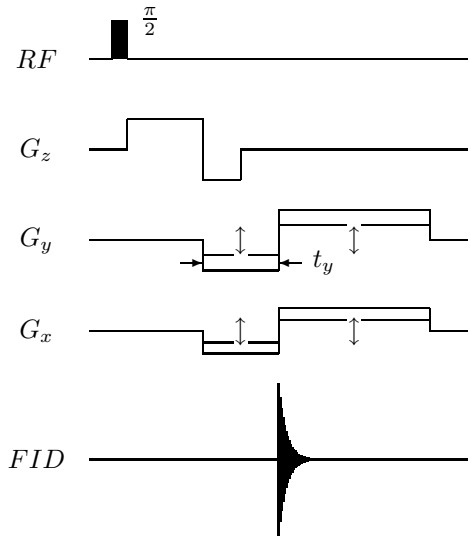

FIGURE 3.11
MR signal detection and demodulation in the radial k-space sampling.

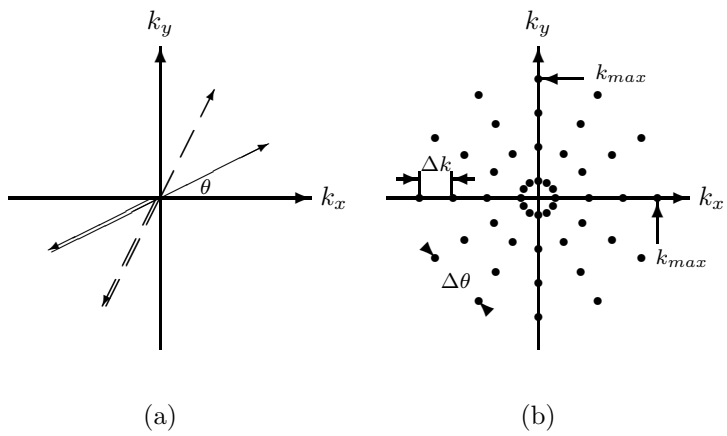

FIGURE 3.12
The trajectory (a) and the sampling (b) in the radial k-space sampling.

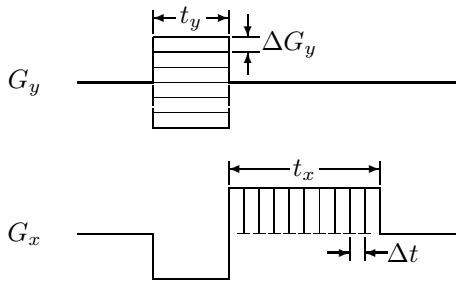

FIGURE 3.13
Phase encoding, frequency encoding, and readout sampling.

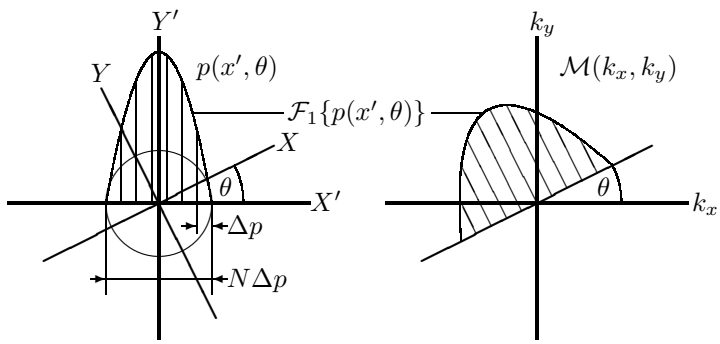

FIGURE 3.14
An illustration of Fourier Slice theorem.

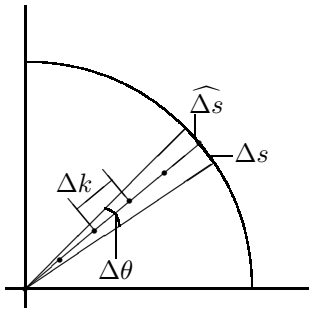

FIGURE 3.15
An illustration of the relationship between M and N in FBP. Because M is large, the arc $\widehat{\Delta s}$ and the chord Δs are very close. They are nearly overlapped on each other and are not virtually distinguished in this figure.

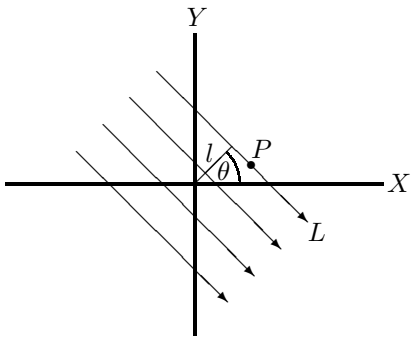

FIGURE 3.16
The geometry of Radon space.

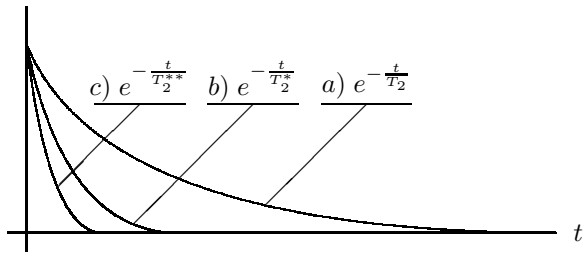

FIGURE 3.17
Three types of decays of FID signal: a) with the intrinsic T_2, b) with T_2^* caused by the inhomogeneities δB_o of the main magnetic field B_o, and c) with T_2^{**} caused by the gradient field B_G.

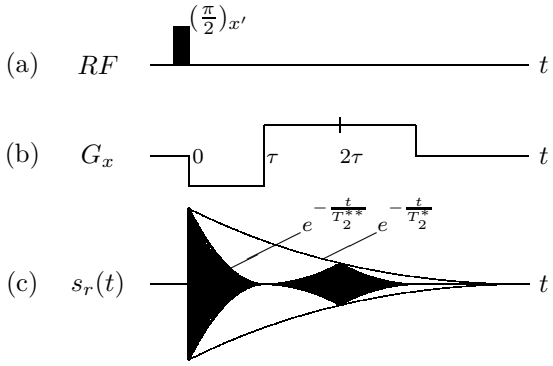

FIGURE 3.18
The gradient echo generation. (a) an excitation RF pulse $(\frac{\pi}{2})_{x'}$, (b) the gradient G_x, (c) the decays of FID signal with T_2^* and T_2^{**}.

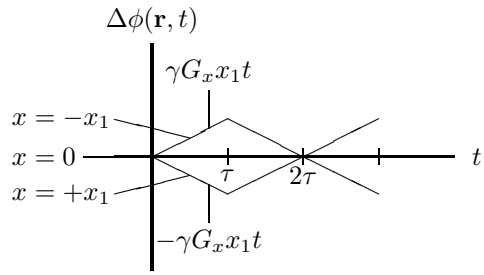

FIGURE 3.19
Phase progressions of spins at three locations $x = x_1,\ 0,\ -x_1$ in the gradient echo.

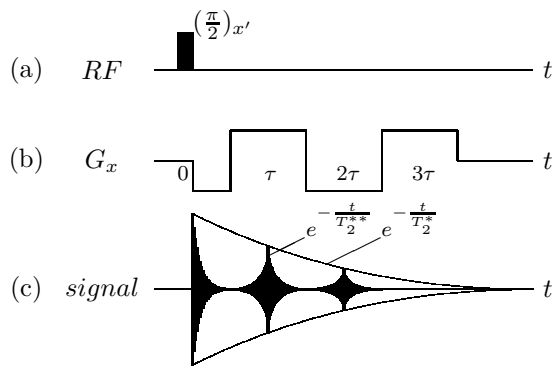

FIGURE 3.20
The gradient echo train generated by switching polarity of the gradient $\vec{G}_x$.

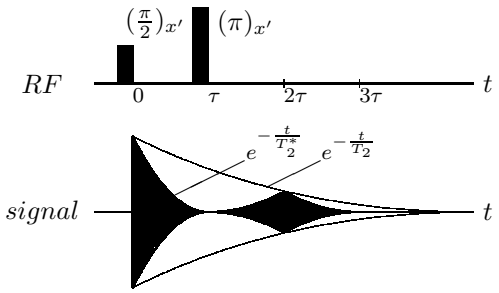

FIGURE 3.21
Spin echo generation by RF pulses $(\frac{\pi}{2})_{x'} - \tau - (\pi)_{x'} - 2\tau$.

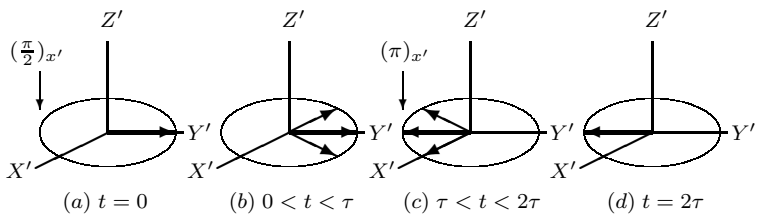

FIGURE 3.22
Phase diagram of TPMM. (a) at $t = 0$, TEMM is flipped by an excitation RF pulse $(\frac{\pi}{2})_{x'}$ onto y'-direction and becomes a TPMM, (b) for $0 < t < \tau$, TPMM begins to fan out and dephase, (c) for $\tau < t < 2\tau$, TPMM is reversed by a refocusing RF pulse $(\pi)_{x'}$ and continues precession, (d) TPMM is rephased at $-y'$-direction and an echo is formed.

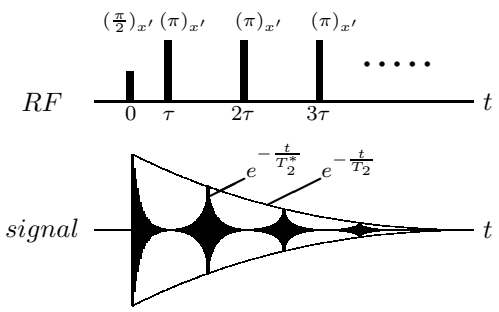

FIGURE 3.23
The spin echo train generated by RF pulse sequence $(\frac{\pi}{2})_{x'} - \tau - (\pi)_{x'}^{(1)} - 2\tau - \cdots - (\pi)_{x'}^{(N)} - 2\tau$.

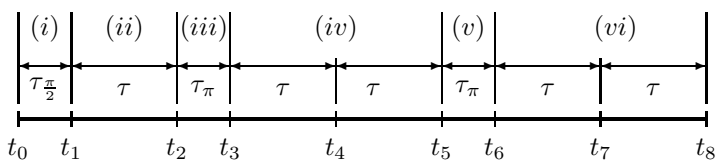

FIGURE 3.24
$(\frac{\pi}{2})_{x'} - \tau - (\pi)_{x'}^{(1)} - 2\tau - (\pi)_{x'}^{(2)} - 2\tau$ pulse sequence generates a process which consists of six sub-processes: (i) an excitation $(t_0 - t_1)$, (ii) a relaxation $(t_1 - t_2)$, (iii) a refocusing $(t_2 - t_3)$, (iv) a relaxation (t_3, t_5), (v) a refocusing (t_5, t_6), and (vi) a relaxation (t_6, t_8).

4

Non-diffraction Computed Tomography

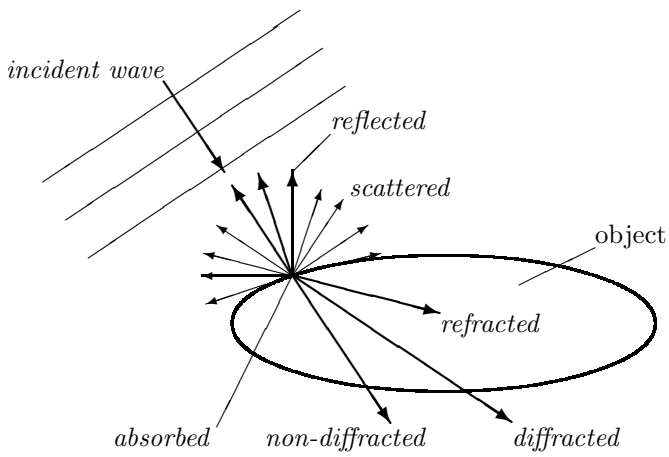

FIGURE 4.1
Physical phenomena caused by interaction between EM wave and an object.

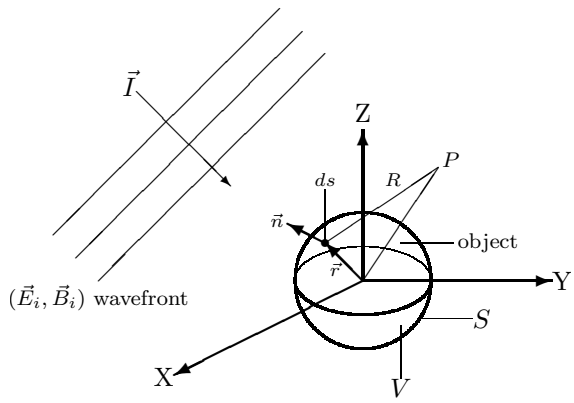

FIGURE 4.2
Incident and scattered waves.

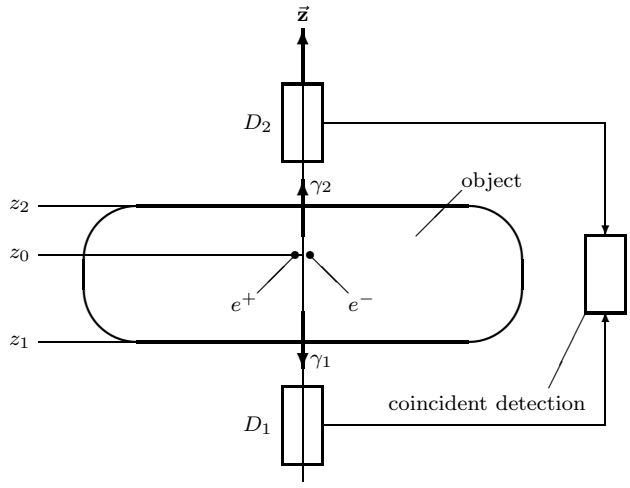

FIGURE 4.3
Illustration of the coincident detection of PET.

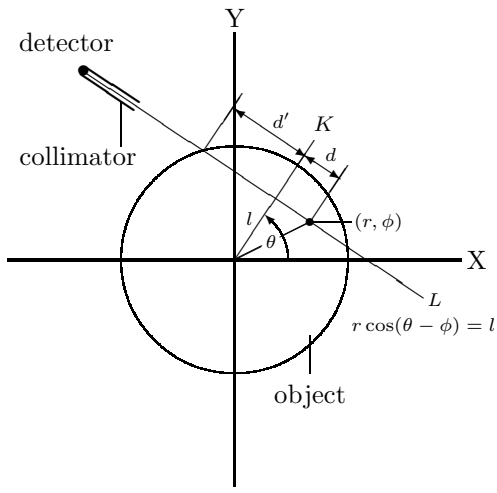

FIGURE 4.4
Illustration of the detection of SPECT.

5

Statistics of x-ray CT Imaging

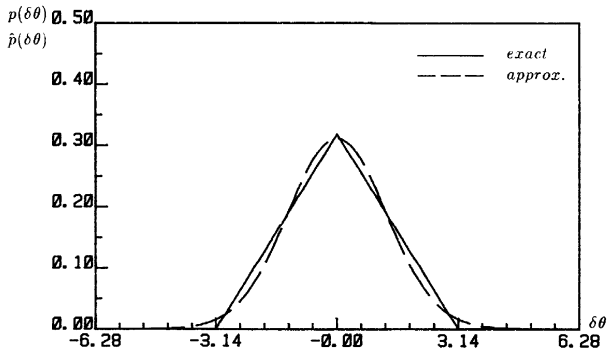

FIGURE 5.1
The true pdf $\hat{p}(\delta\theta)$ and the approximated Gaussian pdf $p(\delta\theta)$ of $\sum_{i=1}^{2} \delta\theta_i$.

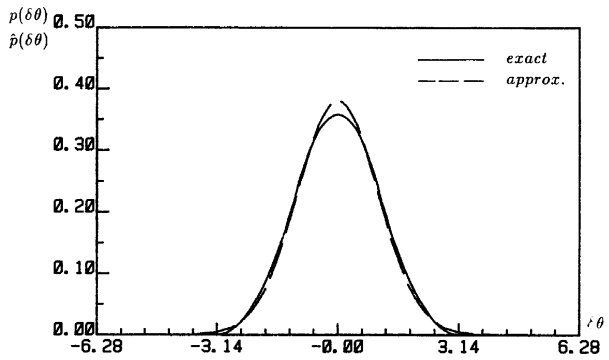

FIGURE 5.2
The true pdf $\hat{p}(\delta\theta)$ and the approximated Gaussian pdf $p(\delta\theta)$ of $\sum_{i=1}^{3} \delta\theta_i$.

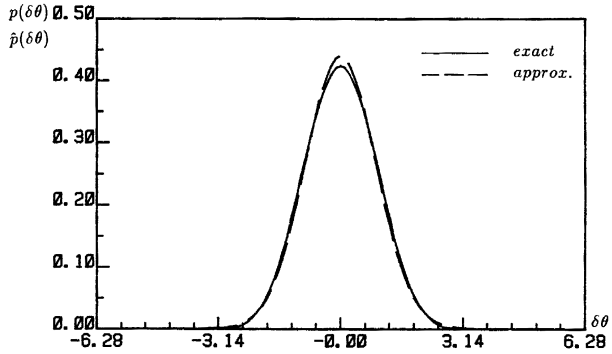

FIGURE 5.3
The true pdf $\hat{p}(\delta\theta)$ and the approximated Gaussian pdf $p(\delta\theta)$ of $\sum_{i=1}^{4} \delta\theta_i$.

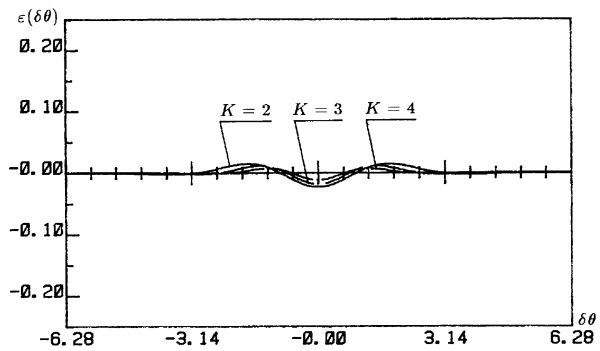

FIGURE 5.4
Differences between the true pdf $\hat{p}(\delta\theta)$ and the approximate Gaussian pdfs $p(\delta\theta)$in the example of (2).

6

Statistics of x-ray CT Image

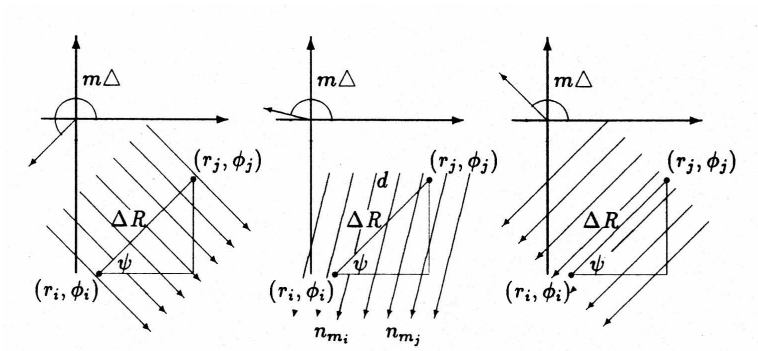

FIGURE 6.1
The geometry of projections and pixel locations.

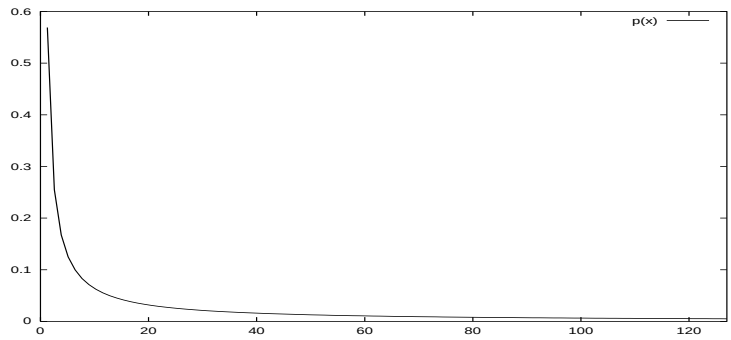

FIGURE 6.2
The relation between the probability $(1 - P_0)$ of two pixel intensities being correlated and the distance ΔR between two pixels.

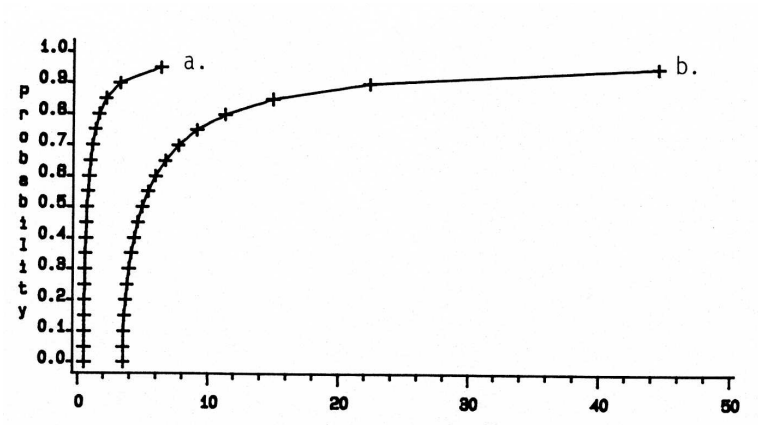

FIGURE 6.3
Relationship between the probability P_0 of two pixel intensities being independent and the pixel separation ΔJ: (a) for parallel projections, (b) for divergent projections.

7

Statistics of MR Imaging

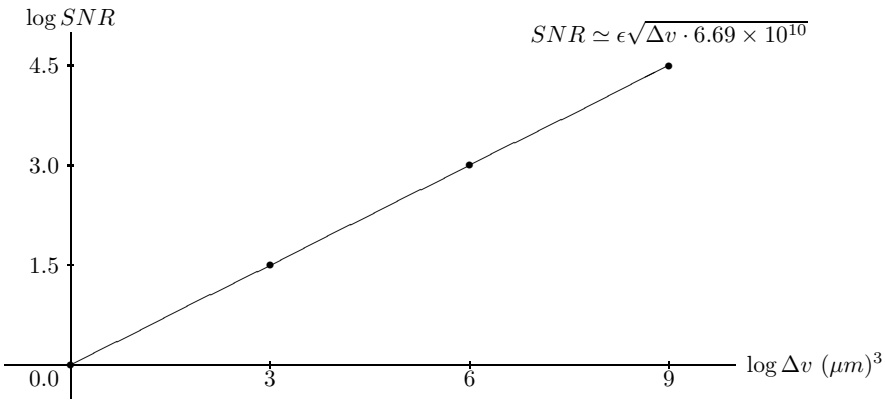

FIGURE 7.1
Relations between spatial resolution Δv and SNR.

8

Statistics of MR Image

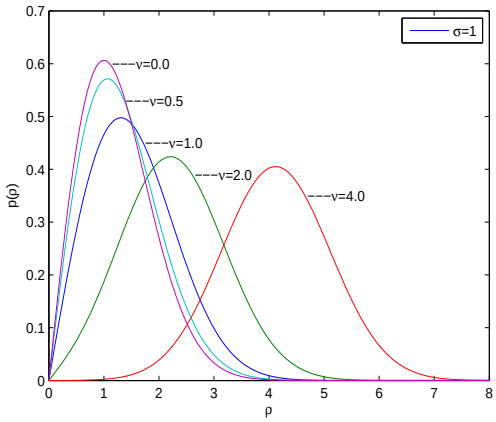

FIGURE 8.1
Rician pdfs (Eq.(8.6)) with various SNR. Among them, Rayleigh pdf (Eq.(8.11)) with the zero SNR, and the approximate Gaussian pdf (Eq.(8.13)) with the moderate or larger SNR.

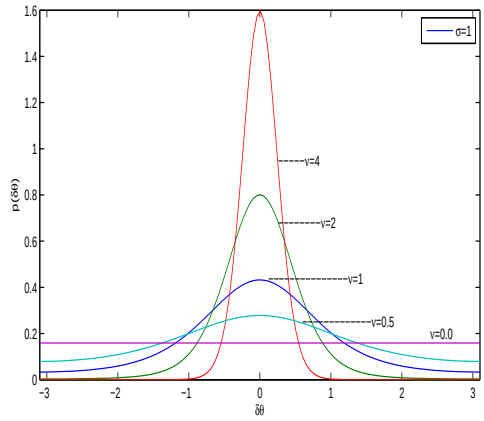

FIGURE 8.2
pdfs Eq.(8.15) with various SNR. Among them, the Uniform pdf (Eq.(8.17)) with the zero SNR, and the approximate Gaussian pdf (Eq.(8.19)) with the moderate or larger SNR.

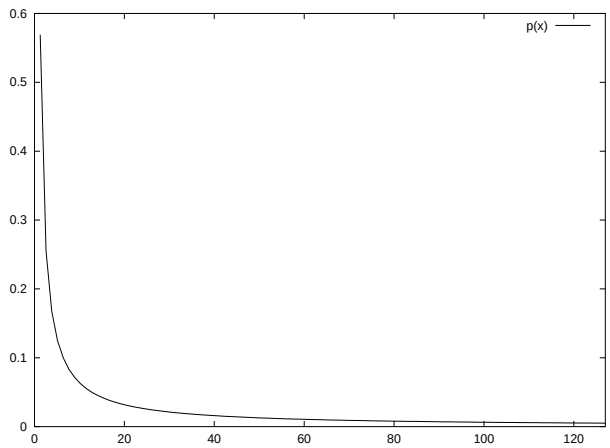

FIGURE 8.3
SAI in PR MR image. For given parameters n_0 and Δp, the probability for two pixel intensities to be correlated, $1 - P_0$ (the vertical axis), is a monotonically decreasing function of the distance between pixels, dr (the horizontal axis): $(1 - P_0) = \frac{2}{\pi} \sin^{-1}(\frac{2n_0 \Delta p}{dr})$.

(a)

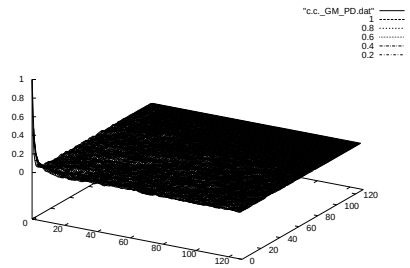

(b)

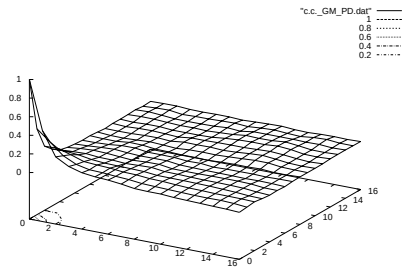

(c)

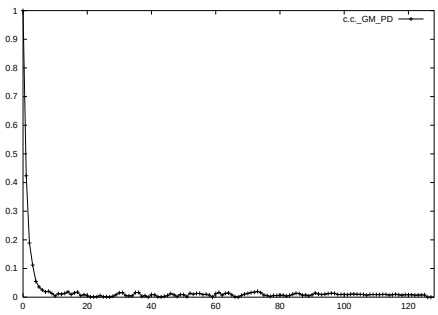

(d)

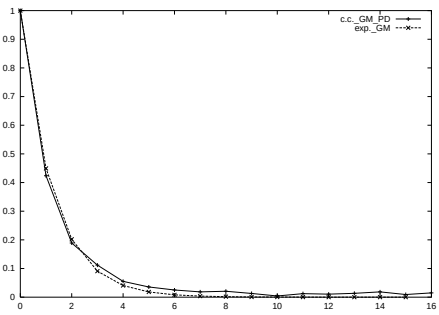

(e)

FIGURE 8.4
ECC of MR image: a) a regional gray matter (GM) image, b) 2-D plot of $|\hat{r}_x(k,l)|$ $(0 \le k, l \le 128)$, c) 2-D plot of $|\hat{r}_x(k,l)|$ $(0 \le k, l \le 16)$, d) 1-D curve of $|\hat{r}_x(0,l)|$ $(0 \le l < 128)$, e) 1-D curves of $|\hat{r}_x(0,l)|$ $(0 \le l < 16)$ (the solid line) and $e^{-0.8 \cdot l}$ (the dash line).

(a)

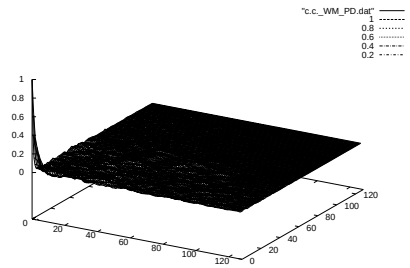

(b)

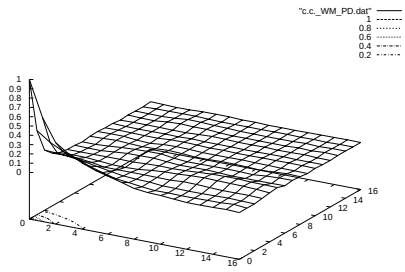

(c)

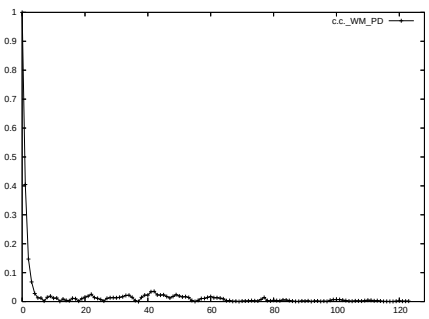

(d)

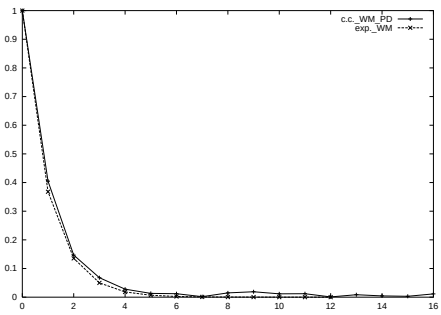

(e)

FIGURE 8.5

ECC of MR image: a) a regional white matter (WM) image, b) 2-D plot of $|\hat{r}_x(k,l)|$ $(0 \le k, l \le 128)$, c) 2-D plot of $|\hat{r}_x(k,l)|$ $(0 \le k, l \le 16)$, d) 1-D curve of $|\hat{r}_x(0,l)|$ $(0 \le l < 128)$, e) 1-D curves of $|\hat{r}_x(0,l)|$ $(0 \le l < 16)$ (the solid line) and $e^{-1.0 \cdot l}$ (the dash line).

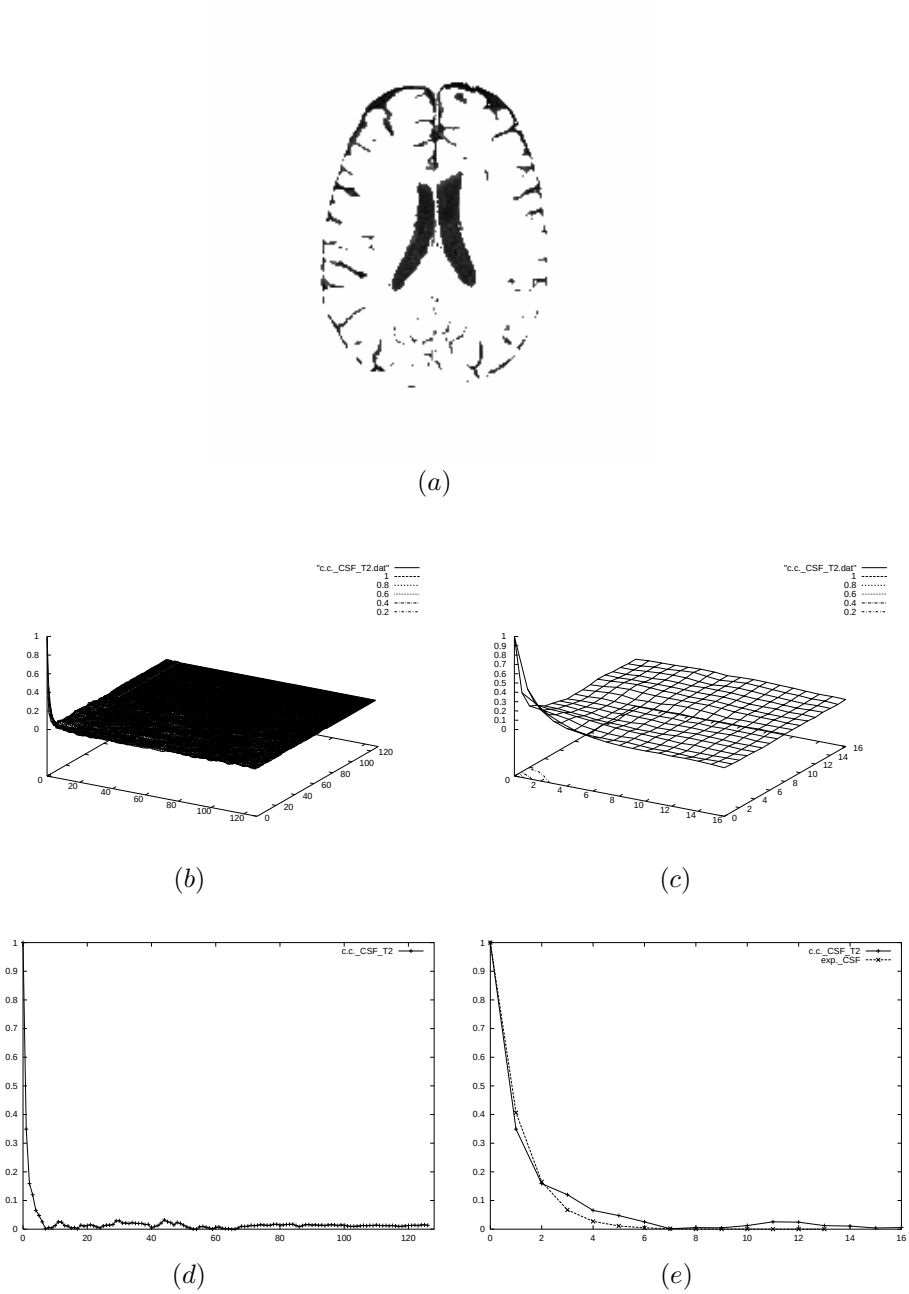

FIGURE 8.6
ECC of MR image: a) regional cerebrospinal fluid (CSF) image, b) 2-D plot of $|\hat{r}_x(k,l)|$ $(0 \le k, l \le 128)$, c) 2-D plot of $|\hat{r}_x(k,l)|$ $(0 \le k, l \le 16)$, d) 1-D curve of $|\hat{r}_x(0,l)|$ $(0 \le l < 128)$, e) 1-D curves of $|\hat{r}_x(0,l)|$ $(0 \le l < 16)$ (the solid line) and $e^{-0.9 \cdot l}$ (the dash line).

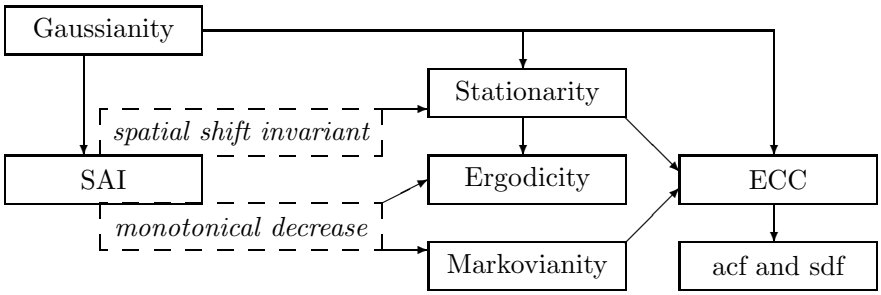

FIGURE 8.7
The inter-relationships in proving six statistical properties of MR image. Markovianity and its proof are given in Chapter 9.

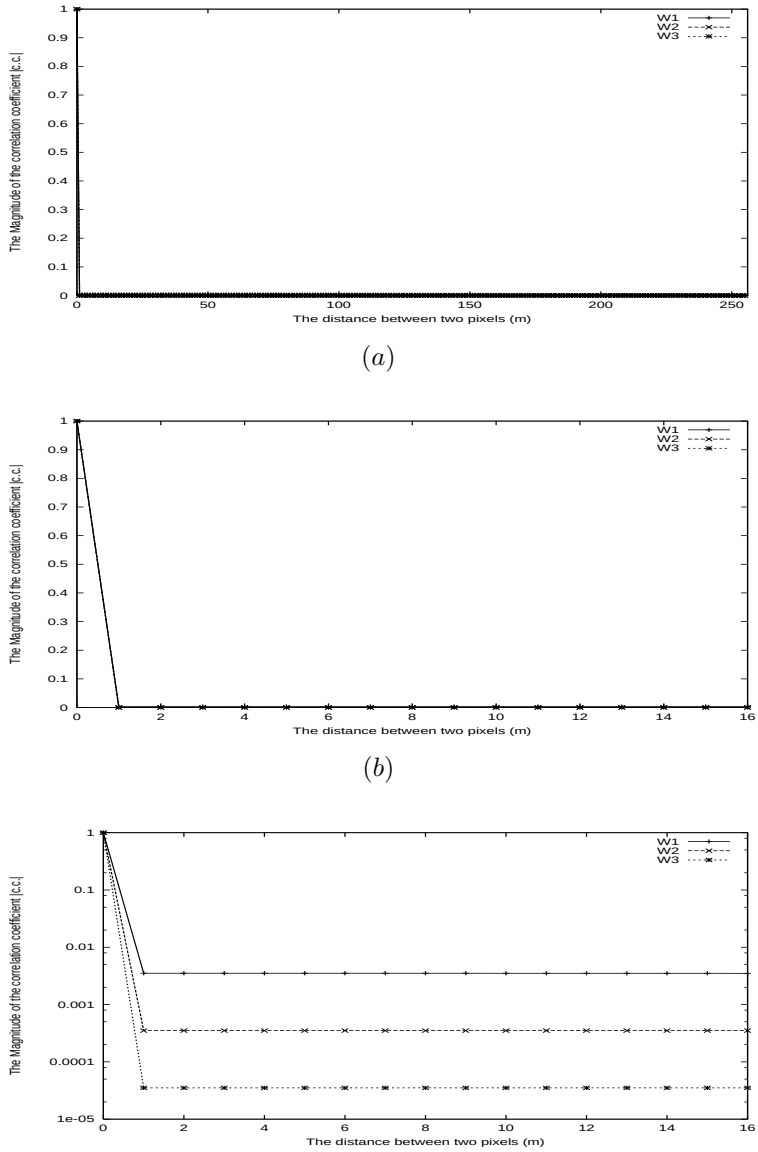

FIGURE 8.8
SAI in the basic FT MR image. $c_{bn}(m)$ of Eq.(8.149) is a measure of the correlation of pixel intensities with respect to the distance between pixels. $N = 256$, $W1 = 255.1\Delta k$, $W2 = 255.91\Delta k$, $W3 = 255.991\Delta k$. Except for the vertical axis in (c) which uses the log scale, all axes in (a)-(c) are the linear scale. (a) $0 \leq m < 256$, (b) $0 \leq m < 16$, (c) $0 \leq m < 16$.

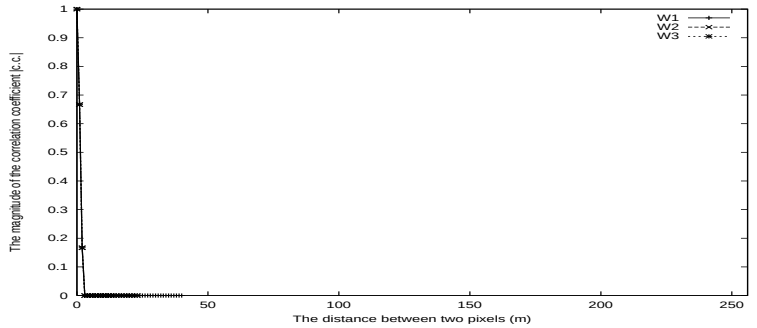

(a)

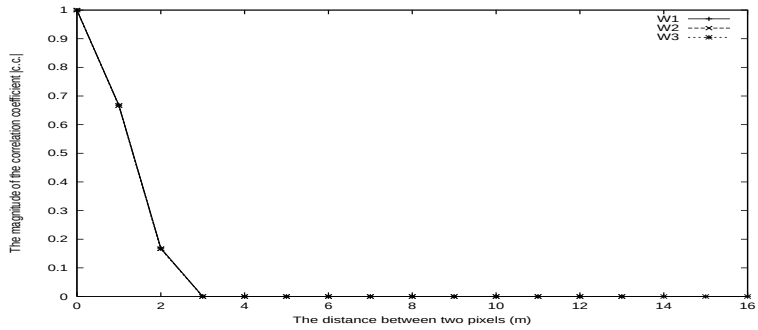

(b)

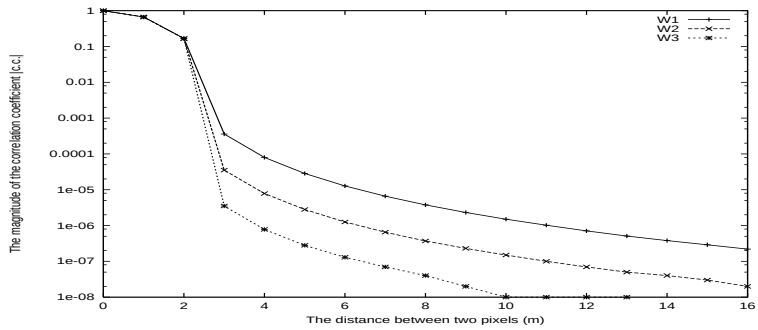

(c)

FIGURE 8.9
SAI in the Hanning-filtered FT MR image. $c_{fn}(m)$ of Eq.(8.154) is a measure of the correlation of pixel intensities with respect to the distance between pixels. $N = 256$, $W1 = 255.1\Delta k$, $W2 = 255.91\Delta k$, $W3 = 255.991\Delta k$. Except for the vertical axis in (c) which uses the log scale, all axes in (a)-(c) use the linear scale. (a) $0 \leq m < 256$, (b) $0 \leq m < 16$, (c) $0 \leq m < 16$.

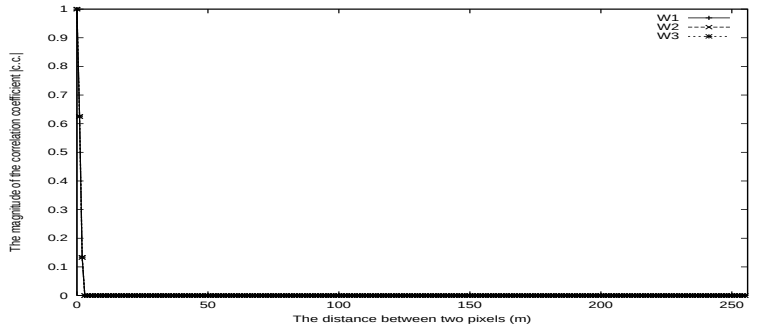

(a)

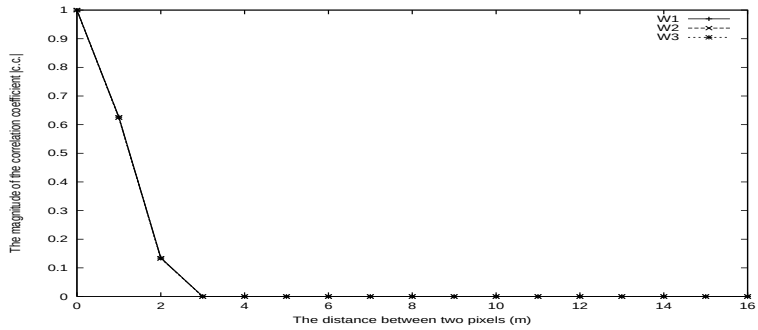

(b)

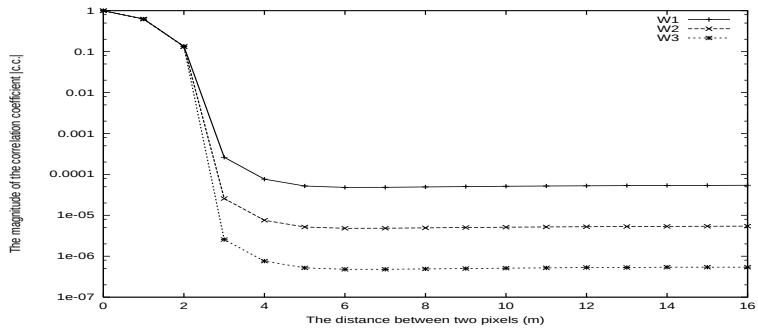

(c)

FIGURE 8.10
SAI in the Hamming-filtered FT MR image. $c_{fn}(m)$ of Eq.(8.154) is a measure of the correlation of pixel intensities with respect to the distance between pixels. $N = 256$, $W1 = 255.1\Delta k$, $W2 = 255.91\Delta k$, $W3 = 255.991\Delta k$. Except for the vertical axis in (c) which uses the log scale, all axes in (a)-(c) use the linear scale. (a) $0 \leq m < 256$, (b) $0 \leq m < 16$, (c) $0 \leq m < 16$.

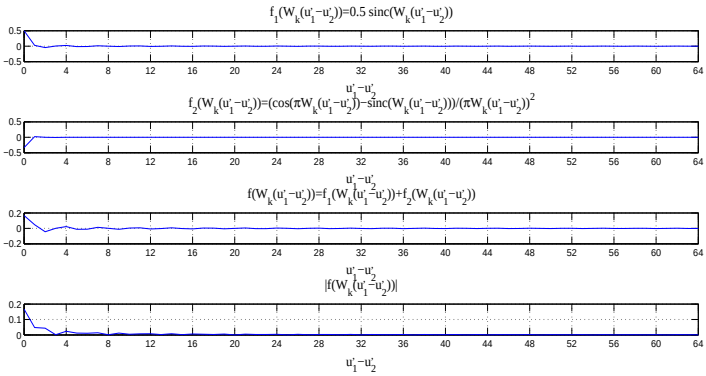

FIGURE 8.11

Simulation results of Eq.(8.160) normalized by $\frac{W_k^3}{2}$, i.e., $f(W_k(u_1' - u_2'))$ of Eq.(8.57) normalized by $\frac{W_k^3}{2}$. (a) the first item $f_1(W_k(u_1' - u_2'))$, (b) the second item $f_2(W_k(u_1' - u_2'))$, (c) $f(W_k(u_1' - u_2'))$ itself, and (d) the magnitude $|f(W_k(u_1' - u_2'))|$.

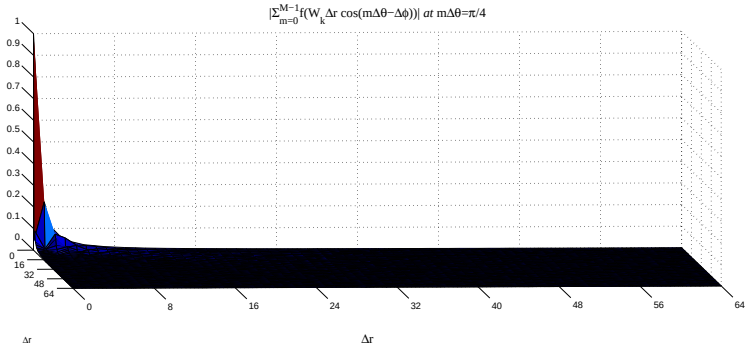

FIGURE 8.12
A 2-D plot of the second item of Eq.(8.162) normalized by $\Delta\theta\frac{\sigma^2_{\mathcal{M}}}{\Delta k}$, i.e., Eq.(8.65) normalized by $\Delta\theta\frac{\sigma^2_{\mathcal{M}}}{\Delta k}$, shows $|\sum_{m=0}^{M-1} f(W_k\Delta r\cos(m\Delta\theta-\phi))|$ monotonically decreases as Δr increases and becomes the almost zero when Δr is large. This simulation result is for a 256×256 image. In its reconstruction, $N = 362$, $M = 569$.

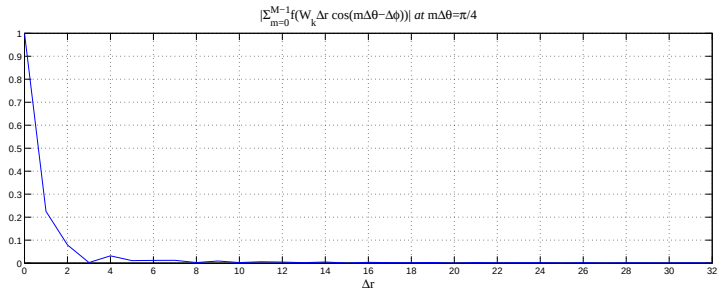

FIGURE 8.13
A line profile in the 2-D plot of Fig.8.12. This line profile is at the view $m\Delta\theta = \frac{\pi}{4}$. It shows that except a few points, e.g., $\Delta r = 3$, $|\sum_{m=0}^{M-1} f(W_k\Delta r\cos(m\Delta\theta-\phi))|$ monotonically decreases as Δr increases and becomes the almost zero for $\Delta r > 8$.

9

Stochastic Image Models

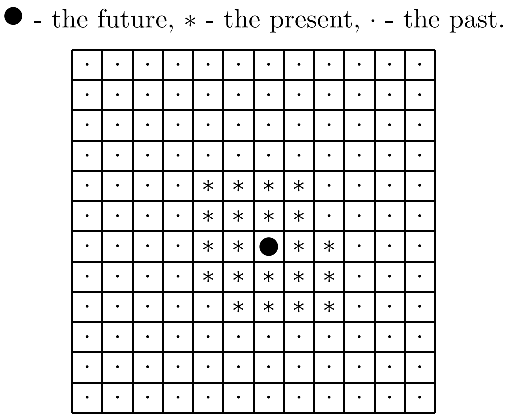

FIGURE 9.1
An illustration of the 2-D lattice and the local dependence $P(\bullet|*, \cdot) = P(\bullet|*)$.

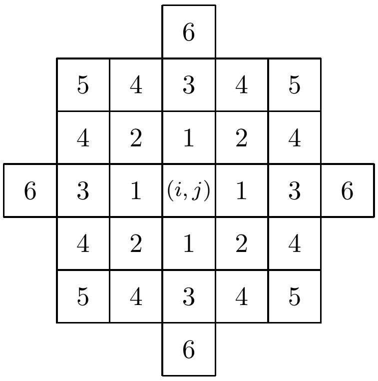

$$\mathcal{N}^p = \{\mathcal{N}^p_{i,j}\} \quad \mathcal{N}^p_{i,j} = \{k : \ k \leq p\}$$

FIGURE 9.2
A structure of neighborhood system up to the 6th order in which the pth order neighborhood system $\mathcal{N}^p$ consists of all lower order systems $\mathcal{N}^k$ $(k < p)$ and additional pixels marked by p.

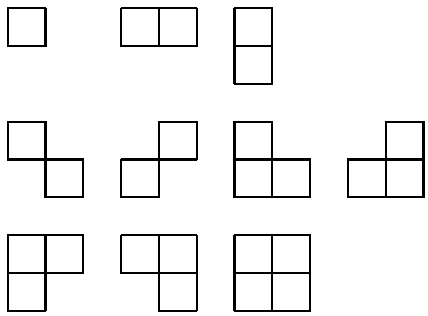

FIGURE 9.3
Clique types in the second order neighborhood system $\mathcal{N}^2$.

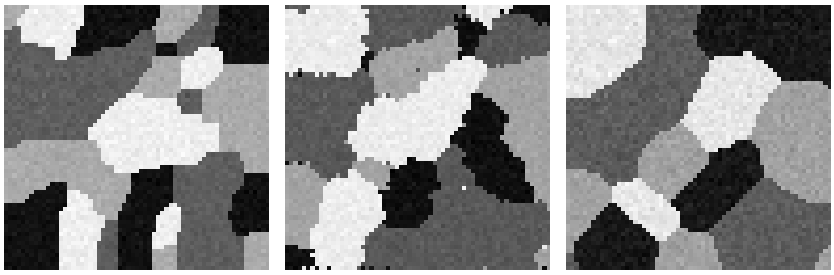

FIGURE 9.4
Examples of MRF configurations generated by using Gibbs sampler.

10

Statistical Image Analysis - I

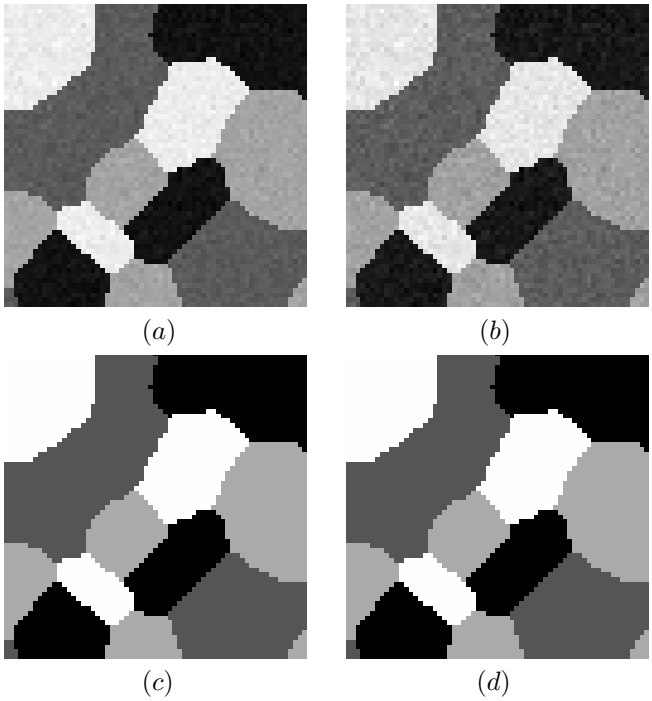

FIGURE 10.1
Two MRF images (a) and (b) with different SNRs. The partitioned region images: the black, dark grey, light grey, and white, (c) and (d).

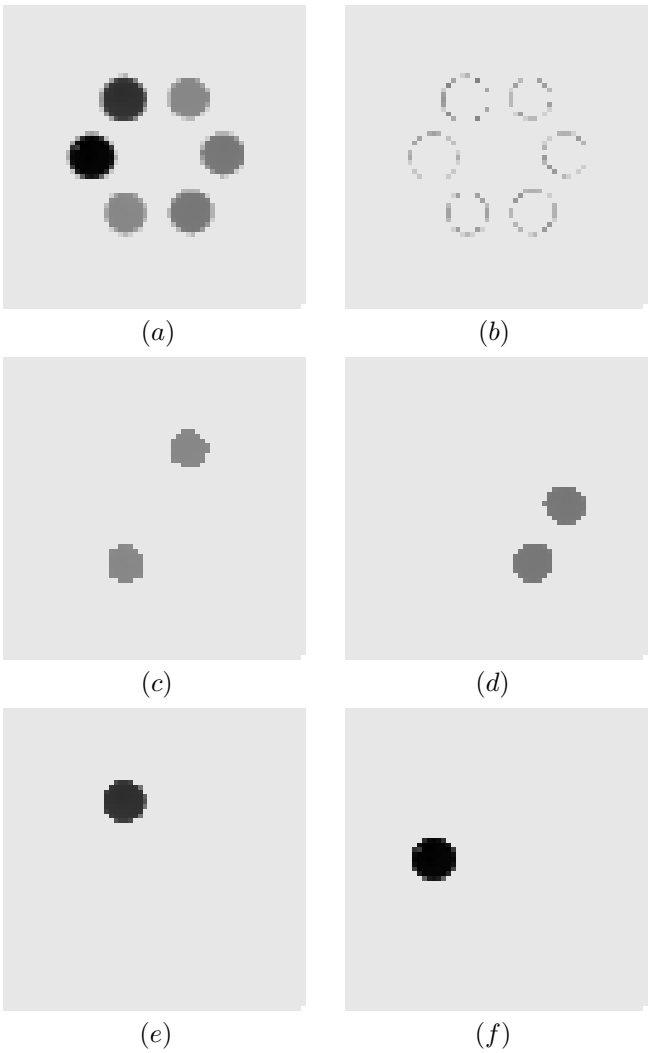

FIGURE 10.2
x-ray CT image of a physical phantom (a). The partitioned region images: (b) Transition zones, (c) Poly (Eth and Prop), (d) 013A(A and B), (e) Teflon, and (f) Bone.

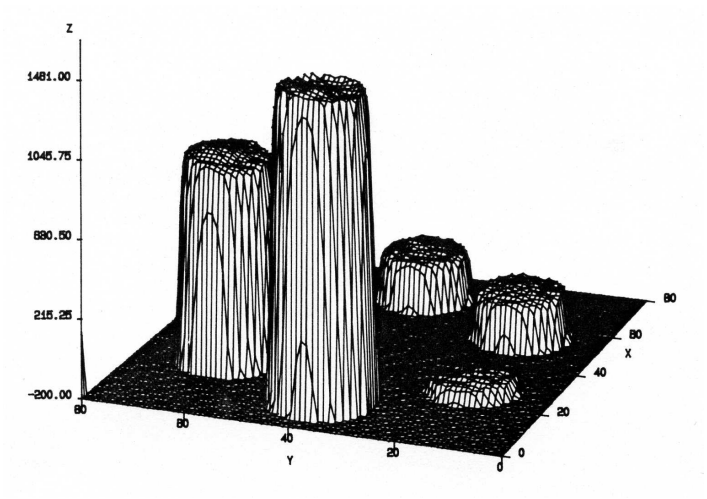

(a)

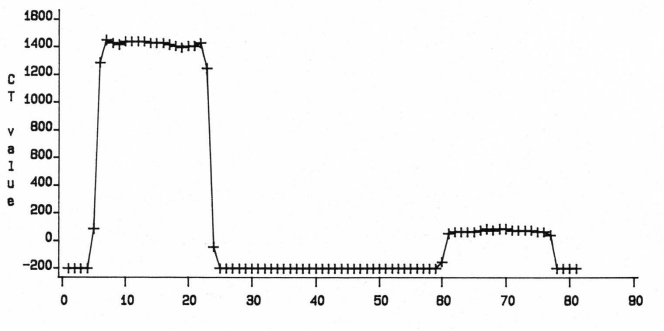

(b)

FIGURE 10.3
(a) A 2-D histogram of the phantom image in Fig.10.2.(a). The flat plateaus represent the homogeneous image regions, the inclined surfaces represent the transition zones between image regions and the background. (b) A line profile at $y = 40$. Several pixels are on the slopping surfaces and form the transition zones.

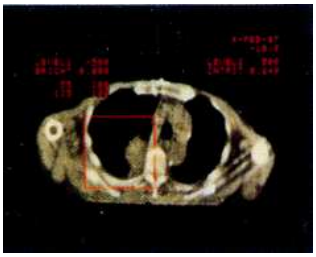

FIGURE 10.4
A cross-sectional x-ray CT image of the chest.

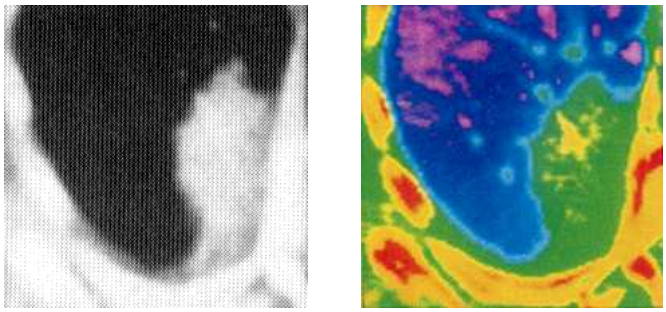

(a) (b)

FIGURE 10.5
An image of the region of interest (ROI) outlined by the red line box in Fig.10.4.

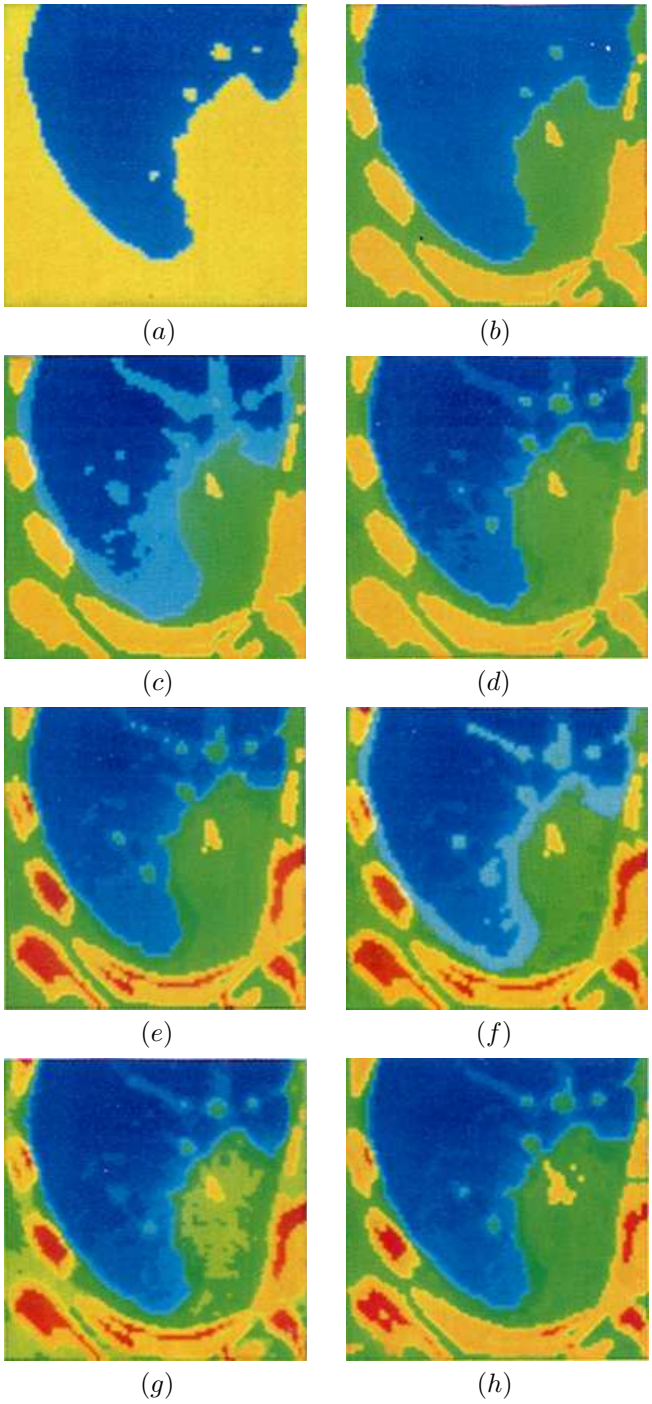

FIGURE 10.6
ROI image of Fig.10.5 is partitioned into $2, \cdots, 8$ region images shown in $(a) \sim (h)$.

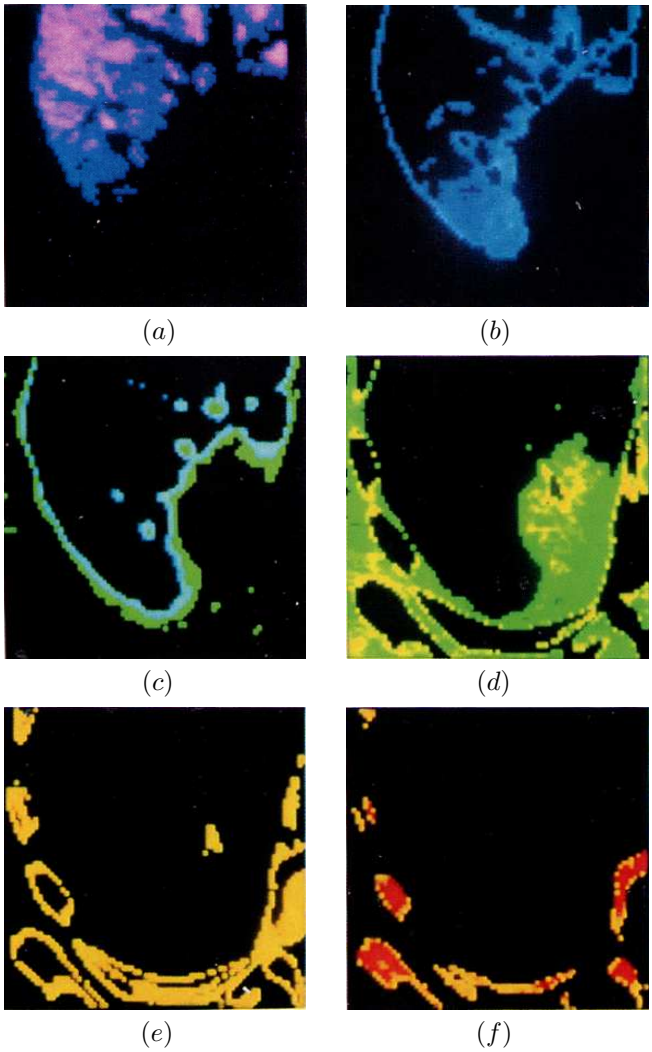

FIGURE 10.7
Images of the 1st, 2nd, 3rd, 4th, 5th, and 6th region image. They represent (a) the lung air, (b) the lung parenchyma and fibrosis, (c) the pleura, blood vessels, and bronchi, (d) a tumor and the tissues outside lung, (e) the dense bone (with a spot of tumor), and (f) the sponge bone.

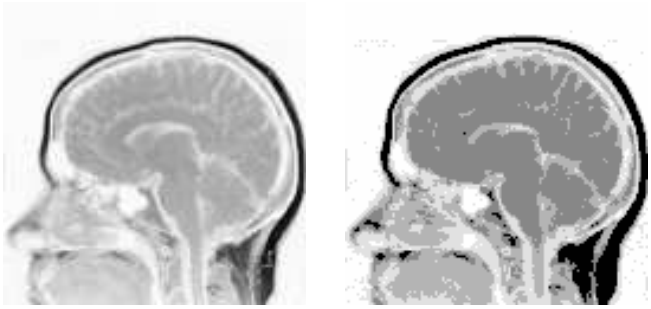

(a) (b)

FIGURE 10.8
A sagittal MR image of the head (a). The partitioned region images are displayed in five grey levels: the white, light grey, grey, dark grey, and black in (b).

11

Statistical Image Analysis - II

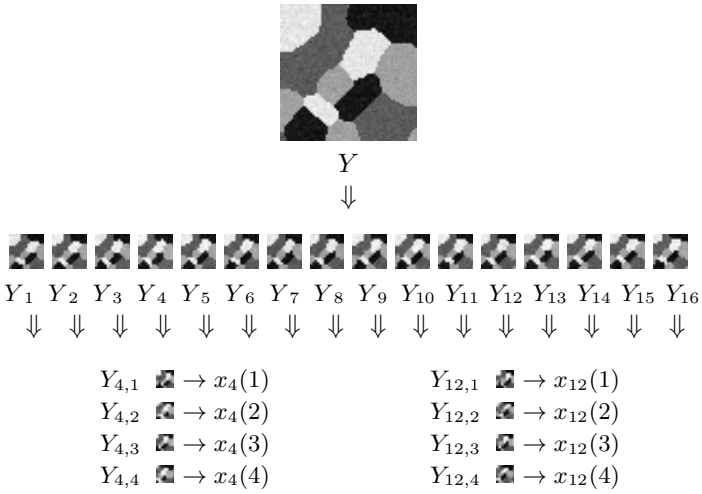

FIGURE 11.1
The first sampling (Eq.(11.3)) creates the sensors, the second sampling (Eq.(11.5)) and the averaging (Eq.(11.6)) form the samples. $x_4(k)$ and $x_{12}(k)$ are shown as examples.

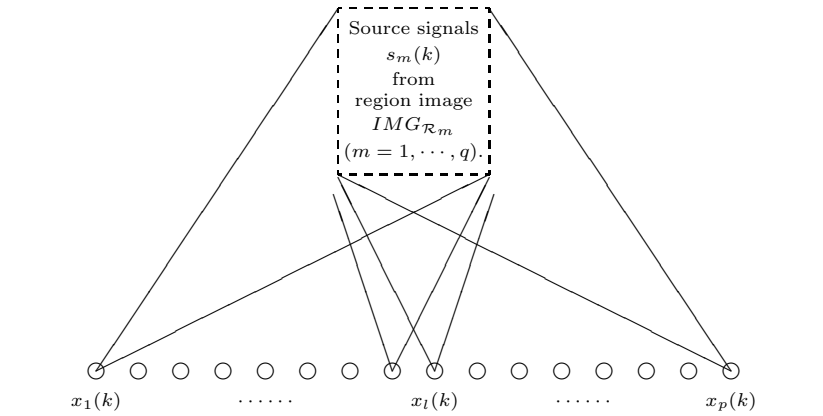

Sensor outputs $x_l(k)$ $(l = 1, \cdots, p)$ are mixtures of source signals $s_m(k)$ $(m = 1, \cdots, q)$.

FIGURE 11.2
An analog sensor array system with q sources and p sensors. Source signals $s_m(k)$ and sensor outputs $x_l(k)$ are related via Eq.(11.9). $x_l(k)$ are computed via Eq.(11.6) and an examples is shown in Fig.11.1.

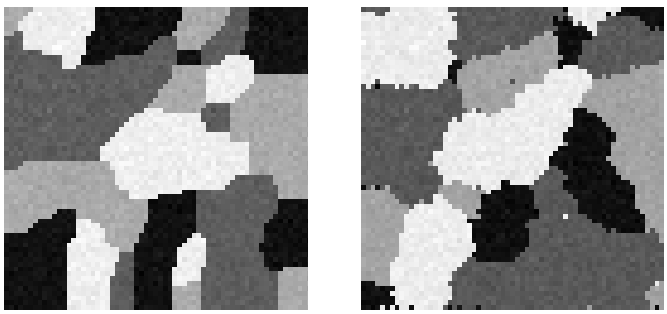

(a) (b)

FIGURE 11.3
Two simulated 64×64 MRF images.

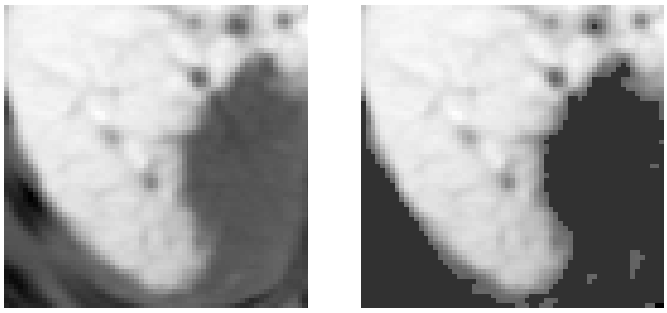

(a) (b)

FIGURE 11.4
x-ray CT image. Two 64×64 ROI images of the lung. The image (a) is original and the image (b) is an image obtained by merging four region images with the higher values of pixel intensities into one region image.

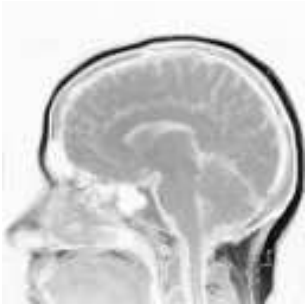

FIGURE 11.5
MR image. A 64×64 sagittal image of the head.

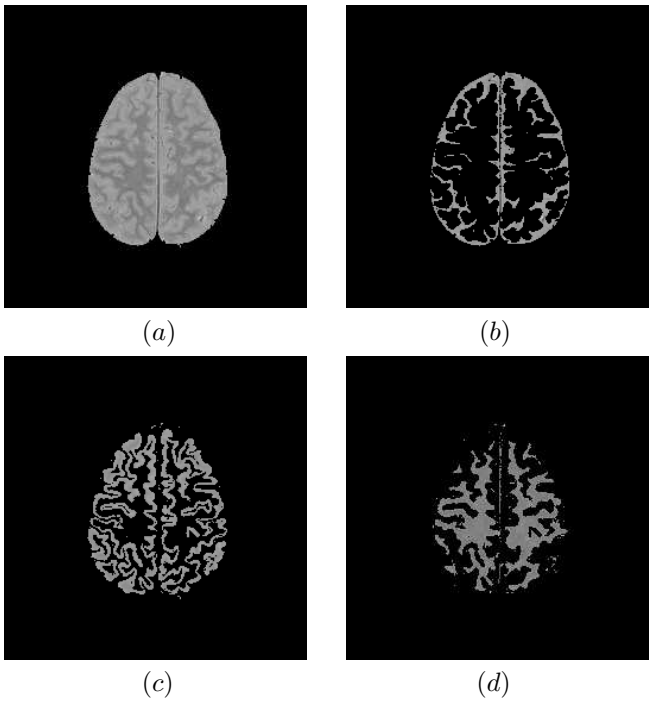

FIGURE 11.6
A Proton Density (PD) weighted MR image of the intracranial (IC) (a), the partitioned region images of the cerebrospinal fluid (CSF) (b), the gray matter (GM) (c), and the white matter (WM) (d).

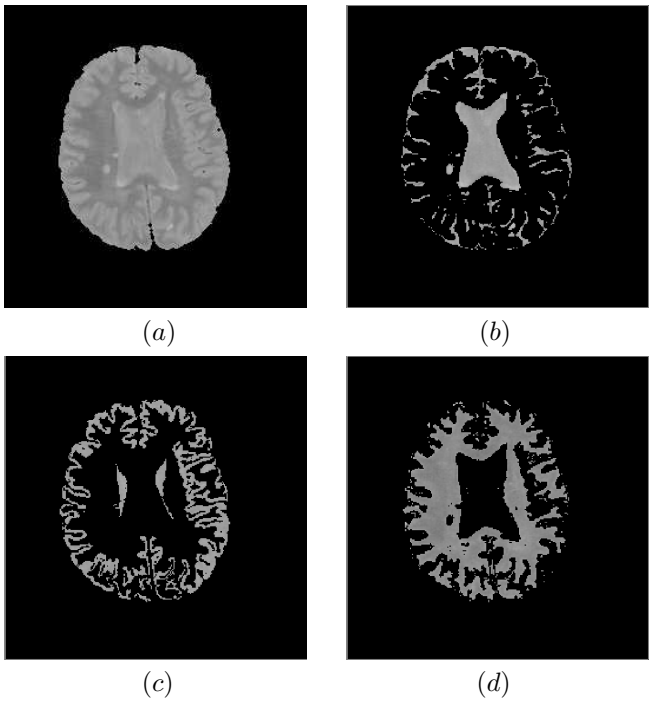

FIGURE 11.7
A Proton Density (PD) weighted MR image of the intracranial (IC) (a), the partitioned region images of the cerebrospinal fluid (CSF) (b), the gray matter (GM) (c), and the white matter (WM) (d).

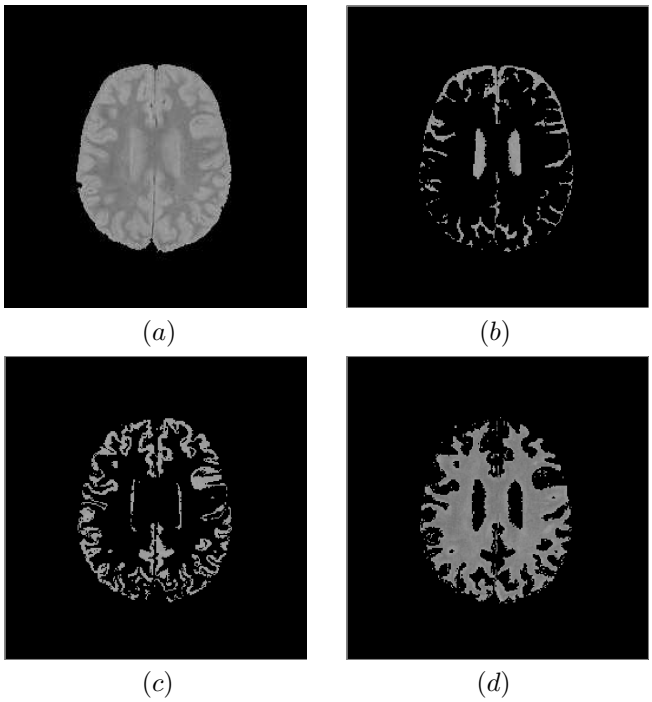

FIGURE 11.8
A Proton Density (PD) weighted MR image of the intracranial (IC) (a), the partitioned region images of the cerebrospinal fluid (CSF) (b), the gray matter (GM) (c), and the white matter (WM) (d).

12

Performance Evaluation of Image Analysis Methods

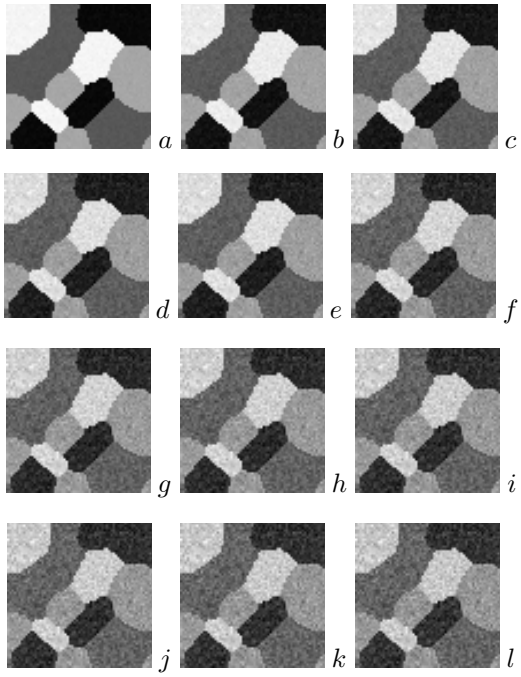

FIGURE 12.1
Twelve simulated images with different variances.

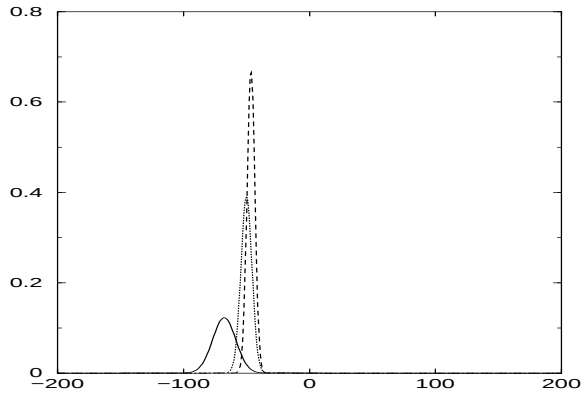

FIGURE 12.2
The pdfs of over-detection in the case $\sigma_0^2 = 10,\ 40,\ 70$ (curves from left to right).

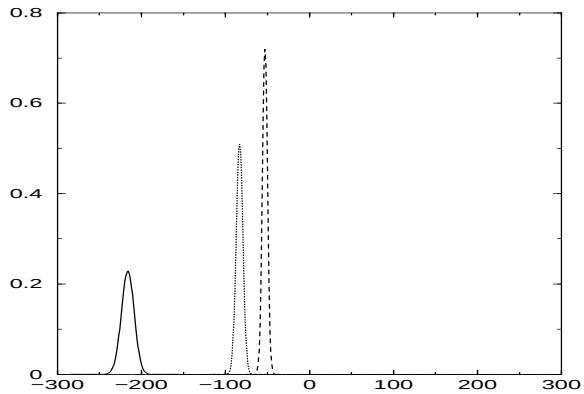

FIGURE 12.3
The pdfs of under-detection in the case $\sigma_0^2 = 10,\ 40,\ 70$ (curves from left to right).

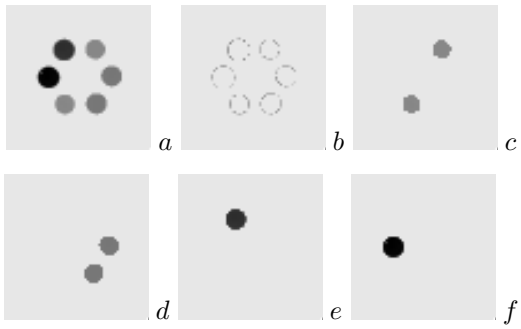

FIGURE 12.4
x-ray CT image of a physical phantom (a) and its 5 components ($b \sim f$).

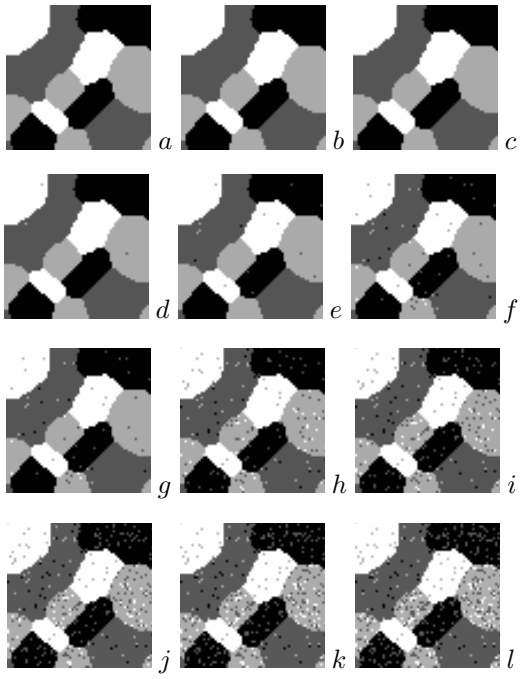

FIGURE 12.5
Partitioned image regions of 12 simulated images shown in Fig.12.1.